Reconstruction of temperature, accumulation rate, and layer thinning from an ice core at South Pole, using a statistical inverse method

Emma C. Kahle[1], Eric J. Steig[1], Tyler R. Jones[2], T.J. Fudge[1], Michelle R. Koutnik[1], Valerie Morris[2], Bruce H. Vaughn[2], Andrew J. Schauer[1], C. Max Stevens[1], Howard Conway[1], Edwin D. Waddington[1], Christo Buizert[3], Jenna Epifanio[3], James W. C. White[2]

[1]Department of Earth and Space Sciences, University of Washington, Seattle WA 98195, USA
[2]Institute of Arctic and Alpine Research, University of Colorado, Boulder CO 80309, USA
[3]College of Earth Ocean and Atmospheric Sciences, Oregon State University, Corvallis OR 97331, USA

Key Points:

- Observations of water-isotope ratios, the gas-ice age difference, and annual-layer thickness are obtained from an ice core at South Pole.
- An inverse method using a firn model with isotope diffusion provides self-consistent temperature, accumulation rate, and thinning histories.
- Novel calibration of the isotope paleothermometer shows that glacial-interglacial temperature change at the South Pole was 6.3 +/- 0.8 K.

Corresponding author: Eric J. Steig, `steig@uw.edu`

Abstract

Data from the South Pole ice core (SPC14) are used to constrain climate conditions and ice-flow-induced layer thinning for the last 54,000 years. Empirical constraints are obtained from the SPC14 ice and gas timescales, used to calculate annual-layer thickness and the gas-ice age difference (Δage), and from high-resolution measurements of water isotopes, used to calculate the water-isotope diffusion length. Both Δage and diffusion length depend on firn properties and therefore contain information about past temperature and snow-accumulation rate. A statistical inverse approach is used to obtain an ensemble of reconstructions of temperature, accumulation-rate, and thinning of annual layers in the ice sheet at the SPC14 site. The traditional water-isotope/temperature relationship is not used as a constraint; the results therefore provide an independent calibration of that relationship. The sensitivity of water isotopes to temperature is greater than previously assumed for East Antarctica. The temperature reconstruction yields a glacial-interglacial temperature change of 6.3±0.8°C at the South Pole.

1 Introduction

Ice cores from polar ice sheets provide important records of past changes in climate and ice dynamics. Temperature and snow-accumulation rate are critical targets for reconstruction from ice-core data (Lorius et al., 1990). The traditional approach to reconstructing temperature is the use of water isotope ratios (δ^{18}O, δD), calibrated using empirical relationships (Dansgaard, 1964; Jouzel et al., 1993). Another approach is borehole thermometry, which provides a direct measurement of the modern temperature profile of the ice sheet that can be related to surface temperature history through a heat advection-diffusion model (Cuffey et al., 1995; Dahl-Jensen et al., 1998). Finally, measurements of δ^{15}N of N_2 in trapped air bubbles provide information about the thickness of the firn layer and past abrupt temperature changes that produce thermal gradients (Sowers et al., 1992; Schwander, 1989; Severinghaus et al., 1998). Because firn thickness is a function of accumulation rate and temperature, δ^{15}N can be used to provide constraints on both variables through modeling of the firn densification process (Huber et al., 2006; Guillevic et al., 2013; Kindler et al., 2014). With independent constraints on the ice-core depth-age relationship, in particular from annual-layer counting, these approaches can be combined to produce robust estimates of temperature and accumulation rate through time. Results from Greenland (Buizert et al., 2014) and the West Antarctic Ice Sheet (WAIS) Divide ice core (Cuffey et al., 2016) provide recent examples.

In comparison with locations in West Antarctica and Greenland, ice-core sites in East Antarctica pose special challenges. The low accumulation rates typical of the East Antarctic plateau are unfavorable for borehole thermometry, which generally requires high accumulation rates and locations near ice divides, where the horizontal velocity is low. Additionally, some recent studies have questioned the validity of firn models at the typically very cold temperatures in East Antarctica (Freitag et al., 2013; Bréant et al., 2017). One approach that may help to address such challenges is to use the "diffusion length", a measure of the spectral properties of high-resolution measurements of water-isotope ratios. Water-isotope diffusion length reflects the vertical diffusion experienced by water molecules through the firn column (Johnsen, 1977; Whillans and Grootes, 1985; Cuffey and Steig, 1998; Johnsen et al., 2000). While diffusion length has primarily been used as a proxy for temperature (e.g., Simonsen et al., 2011; van der Wel et al., 2015; Gkinis et al., 2014; Holme et al., 2018), it is sensitive to both temperature and accumulation rate though their influence on the firn density profile, and is also affected by vertical strain (Gkinis et al., 2014; Jones et al., 2017a). Diffusion length thus provides an independent constraint on several important ice-core properties: temperature, accumulation rate, and the thinning history due to ice deformation.

Here, we present data from a new ice core (SPC14) from the South Pole, East Antarctica, and we use a novel approach to combine multiple data sets to constrain temperature, accumulation-rate, and ice-thinning histories. We take advantage of two timescales for SPC14, one for the ice (Winski et al., 2019) and one for the gas enclosed within it (Epifanio et al., 2020), to obtain an empirical measure of the gas-age ice-age difference (Δage). We also use high-resolution measurements of δ^{17}O, δ^{18}O, and δD of ice to obtain water-isotope diffusion lengths.

We use a statistical inverse approach to obtain optimized, self-consistent reconstructions of temperature and accumulation rate using a combined firn-densification and water-isotope diffusion model. We exclude gas isotope (δ^{15}N) data and use the water-isotope values only for calculating diffusion length, reserving these variables for comparison and validation. This approach allows us to produce a novel and independent calibration of the traditional isotope paleothermometer without the use of borehole thermometry. We also obtain an independent constraint on the thinning of annual layers. This is important at South Pole because the location of the site is about 200 km from the ice divide and the ice-flow history is not well known at ages earlier than the Holocene (Lilien et al., 2018).

2 Data from the South Pole Ice Core

The South Pole Ice Core (SPC14) was obtained from 2014 to 2016 at 89.9889°S, 98.1596°W, approximately 2 km from the geographic South Pole. SPC14 was drilled to a depth of 1751 m, equivalent to an age of approximately 54 ka (Winski et al., 2019). Compared to other East Antarctic ice-core sites, South Pole has a relatively high annual accumulation rate (8 cm w.e. yr^{-1}) (Casey et al., 2014) given its low mean-annual air temperature of -49°C (Lazzara et al., 2012). The mean firn temperature is -51°C (Severinghaus et al., 2001). The modern surface ice velocity is 10 m yr^{-1} (Casey et al., 2014).

The data sets used in our analysis are developed from the independent ice and gas timescales for SPC14 described previously by Winski et al. (2019) and Epifanio et al. (2020), and water-isotope measurements presented here for the first time. We briefly summarize the information obtained directly from the ice-core measurements as well as the data sets derived from that information (annual-layer thickness, Δage, and water-isotope diffusion length).

2.1 Ice Timescale and Annual-Layer Thickness

The ice timescale was constructed by stratigraphic matching of 251 volcanic tie points between SPC14 and WAIS Divide (Winski et al., 2019). Between tie points, identification of individual layers from seasonal cycles in sodium and magnesium ions was used to produce an annually-resolved timescale for most of the Holocene. For ages greater than 11.3 ka, despite lack of annual resolution, the uncertainty of the timescale is estimated to be within 124 years relative to WD2014 (Winski et al., 2019). Annual-layer thickness is given by the depth between successive years on the SP19 timescale. For ages older than 11.3 ka where annual layers could not be identified, Winski et al. (2019) found the smoothest annual-layer thickness which matched 95% of the volcanic tie points to within one year. Based on the uncertainty associated with interpolation between sparse tie points (Fudge et al., 2014), we estimate the uncertainty in annual-layer thickness (two standard deviations, hereafter s.d.) to be ±3% of the value in the Holocene, increasing to ±10% of the value at earlier ages.

2.2 Gas Timescale and Δage

Epifanio et al. (2020) developed the SPC14 gas timescale through stratigraphic matching of features in the high-resolution CH_4 records of the SPC14 and WAIS Divide cores. The difference in age between the ice and gas timescales, Δage, is a measure of the ice age at the lock-in depth, which depends on the rate of firn densification (Schwander et al., 1984,9; Blunier and Schwander, 2000). Epifanio et al. (2020) determined Δage empirically at each of the CH_4 tie points and used a cubic spline fit to derive a continuous Δage curve for all depths. Due to the empirical nature of the gas timescale, the SPC14 Δage record is determined without the use of a firn-densification model. Moreover, the SPC14 Δage was obtained without relying on the additional constraint of δ^{15}N to determine lock-in depth.

We assign an age to each empirical Δage estimate as the mid-point between the gas-age and ice-age timescales from which Δage is calculated. This approximation is justified by results from a dynamic densification model (Stevens et al., 2020), which show that at a site like South Pole the timescale on which Δage responds to climate variations is a time interval shorter than Δage itself. Uncertainty in Δage depends on uncertainty in the match between the WAIS Divide and SPC14 gas timescales, the uncertainty associated with interpolation between tie points, and uncertainty in the Δage for WAIS Divide. Because Δage is an order of magnitude smaller at WAIS Divide than at South Pole, that source of uncertainty is the smallest. The uncertainty estimated by Epifanio et al. (2020) ranges from ±1% to ±8% (two s.d.) of the value of Δage.

2.3 Water-Isotope Measurements and Diffusion Length

We measured water-isotope ratios at an effective resolution of 0.5 cm using continuous flow analysis (CFA), following the methods described in Jones et al. (2017b). We measured δ^{18}O and δD for the entirety of the core and δ^{17}O from a depth of 556 m through the bottom of the core. We used Picarro Inc. cavity ring-down laser spectroscopy (CRDS) instruments, including both a model L2130-i (for δ^{18}O and δD) and a model L2140-i for δ^{17}O (Steig et al., 2014). We use the standard notation for δ^{18}O:

$$\delta^{18}O_{sample} = \left(\frac{^{18}O}{^{16}O}\right)_{sample} \Big/ \left(\frac{^{18}O}{^{16}O}\right)_{VSMOW} - 1,$$

where VSMOW is Vienna Standard Mean Ocean Water. δ^{17}O and δD are defined similarly. These measurements were used to calculate the water-isotope diffusion length. Figure 1 shows the δ^{18}O measurements at 100-year-mean resolution as a function of age.

After deposition as snow on the ice-sheet surface, water isotopologues diffuse through interconnected air pathways among ice grains in the firn, driven by isotope-concentration gradients in the vapor phase (Johnsen, 1977; Whillans and Grootes, 1985; Cuffey and Steig, 1998). In solid ice below the firn column, diffusion continues, but at a rate orders of magnitude slower than in the firn (Johnsen et al., 2000). The extent of diffusion is quantified as the diffusion length, the mean cumulative diffusive-displacement in the vertical direction of water molecules relative to their original location in the firn.

Diffusion length is determined from spectral analysis of the high-resolution water-isotope data, following the methods described in Kahle et al. (2018). We use discrete data sections of 250 years. We calculate the diffusion length, σ, for each section by fitting its power spectrum with a model of a diffused power spectrum and a two-component model of the measurement system noise:

$$P = P_0 \exp(-k^2\sigma^2) + P_0' \exp(-k^2(\sigma')^2) + |\hat{\eta}|^2, \tag{1}$$

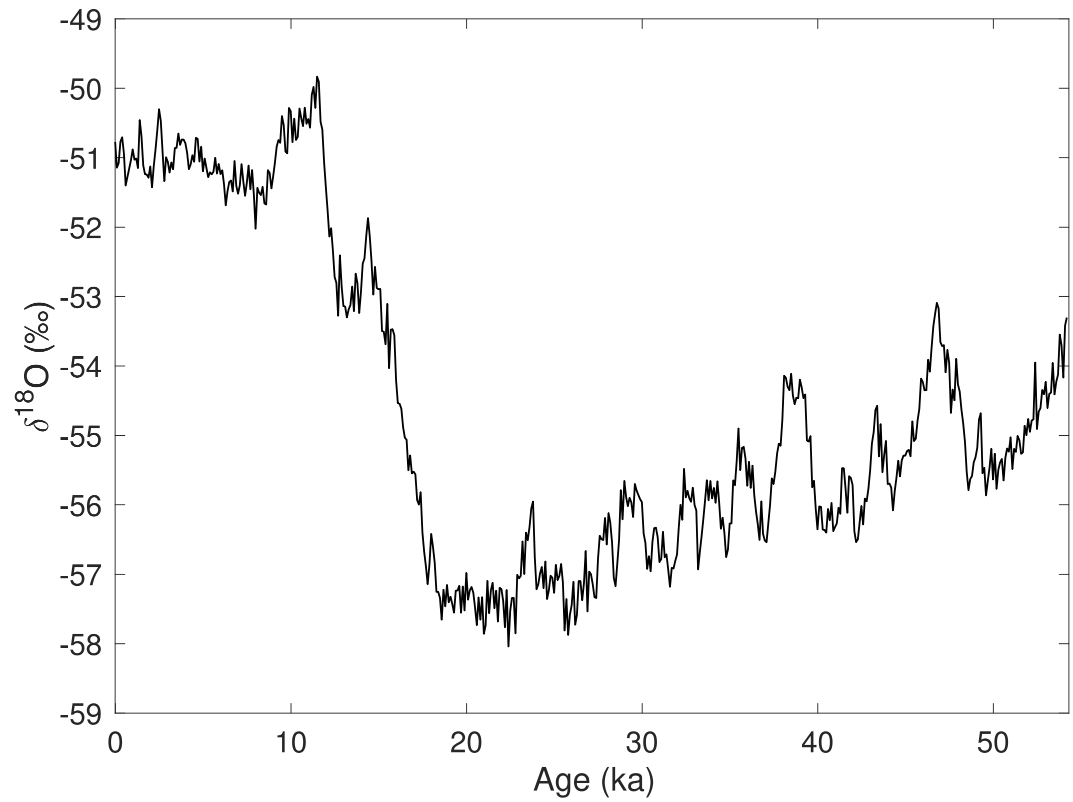

Figure 1: High-resolution δ^{18}O record from the South Pole ice core (SPC14), shown as discrete 100-year averages for clarity, on the SP19 ice timescale (Winski et al., 2019).

where k is the wavenumber, $|\hat{\eta}|^2$ is the measurement noise, and P_0, P_0', and σ' are variable fitting parameters. The second term ($P_0' \exp(-k^2(\sigma')^2)$) accounts for the influence of the CFA measurement system on the water-isotope data spectrum. Kahle et al. (2018) found that this term does not completely eliminate the effect of system smoothing on the spectrum; we therefore make an additional correction, based on the sequential measurement of ice standards of known and differing isotopic composition, following Jones et al. (2017b). This correction is small, accounting for only $\sim$4% of the total diffusion length throughout the core. The uncertainty on σ is estimated conservatively as described in Kahle et al. (2018) and varies from $\pm$4% to $\pm$66% (two s.d.) of the value throughout the core.

Additionally, we correct the diffusion-length estimates to account for diffusion in the solid ice, following Gkinis et al. (2014). This effect is also small, accounting for a maximum of 4% of the total diffusion length at the bottom of the core. To calculate the solid-ice diffusion length, we assume the modern borehole temperature profile $T(z)$ remains constant through time to find the diffusivity profile $D_{ice}(z)$, following Gkinis et al. (2014). We use borehole temperature measurements from the nearby neutrino observatory (Price et al., 2002). We assume a simple thinning function from a 1-D ice-flow model (Dansgaard and Johnsen, 1969) with a kink-height $h_0 = 0.2$ for this calculation; the error in this assumption is negligible for the small deviations in total thinning we are calculating. We subtract both the solid-ice and CFA diffusion lengths from the observations in quadrature to produce our final diffusion-length data set. Further details on both corrections are provided in the Supporting Information.

We calculate the diffusion length for each of the three water-isotope ratios measured on the core. To combine the information from each isotope, we convert δ^{17}O and δD diffusion lengths to equivalent values for δ^{18}O. For example, the δ^{18}O-equivalent diffusion length ($\sigma_{18\,from\,17}$) from the δ^{17}O diffusion length (σ_{17}) is:

$$\sigma^2_{18\,from\,17} = \sigma^2_{17}\ \frac{D_{18}}{\alpha_{18}} \Big/ \frac{D_{17}}{\alpha_{17}}, \tag{2}$$

where D and α are the corresponding air diffusivity and solid-vapor fractionation factor for each isotope. Values for D and α are given in the Supporting Information (Majoube, 1970; Barkan and Luz, 2007; Luz and Barkan, 2010; Lamb et al., 2017). For the single diffusion-length record used in our analysis, we take the mean of these three estimates for σ_{18}.

3 Forward Model

We use a forward model to relate the observational data sets to the variables of interest. Figure 2 summarizes the data sets obtained from the ice-core measurements and the calculations described above: Δage, water-isotope diffusion length, and annual-layer thickness. We use these three data sets as our "observations" in a statistical inverse approach to infer temperature, accumulation rate, and ice-thinning function.

Figure 3 illustrates the structure of the forward model, including a firn-densification component, a water-isotope diffusion component, and a vertical strain (ice thinning) component. We describe the individual components below.

3.1 Firn Densification

The firn layer comprises the upper few tens of meters of the ice sheet where snow is progressively densifying into solid ice. As successive layers of snow fall on the surface of the ice sheet, the increase in overburden pressure causes the underlying ice crystals to pack closer together. The rate of densification is determined primarily by temperature and accumulation rate. The Herron and Langway (1980) (HL) firn-densification model is the benchmark empirical model, based on depth-density data from Greenland and Antarctic ice cores. We model the depth-density profile of the firn using the HL framework due to its simplicity and its good match with measurements of the modern South Pole firn density.

We use a surface density $\rho_0 = 350$ kg m^{-3}, consistent with measured values at the SPC14 site, and assume it remains constant through time (Fausto et al., 2018). The bottom of the firn is constrained by a close-off density ρ_{co}, which we define as a function of temperature (Martinerie et al., 1994). As temperature varies between -50 and -60°C, close-off density varies in a small range between 831.5 and 836.4 kg m^{-3}.

We use the analytical formulation of the HL model, which assumes an isothermal firn. If either temperature or accumulation rate changes on short timescales, a transient formulation of the model would be required to reflect propagation through the firn column. Although our temperature and accumulation-rate inputs vary through time, the timescale of those variations (*e.g.* 10 ka for ∼6°C change in temperature) is large enough that the steady-state approximation is acceptable. To test this assumption, we ran our forward model with a transient formulation of the HL model (Stevens et al., 2020) and found no difference in the results. Since the transient model is more computationally expensive, we use the analytical formulation.

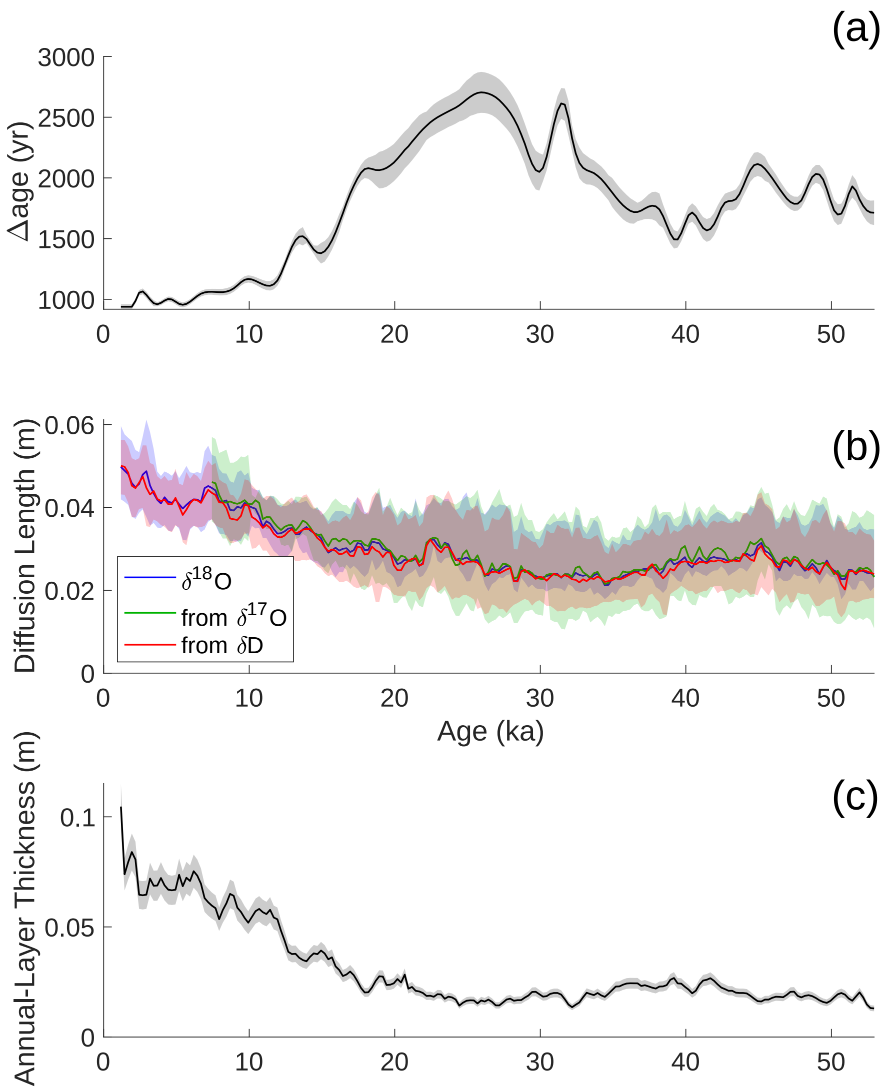

Figure 2: Data sets from SPC14 used to optimize the inverse problem, each averaged over bins of 250 years and plotted with uncertainty representing two s.d. Panel (a) shows annual-layer thickness data, panel (b) shows Δage, and panel (c) shows water-isotope diffusion lengths. Diffusion lengths from δ^{17}O (green) and δD (red) have been converted to δ^{18}O-equivalent values.

3.2 Modeling Δage

Modeled Δage is given by the difference in the modeled age of the ice and the gas at the lock-in depth. We define the lock-in depth at a density of 10 kg m^{-3} less than the close-

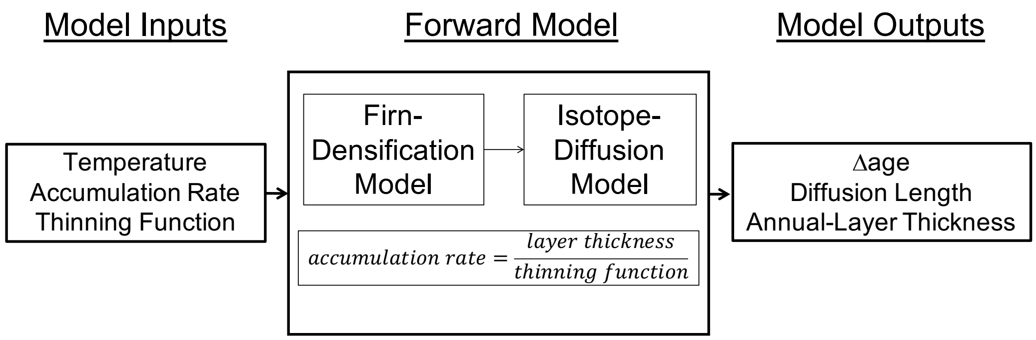

Figure 3: Illustration of the forward model, which includes firn densification, water-isotope diffusion, and vertical strain. Together, these components relate the variables of interest (temperature, accumulation rate, and thinning function) to the observational data sets (Δage, layer thickness, and diffusion length) shown in Figure 2.

off density (Blunier and Schwander, 2000). The age of the ice at this depth is estimated directly from the depth-density profile. We estimate the age of the gas at the lock-in depth (LID) using the parameterization in Buizert et al. (2013):

$$\text{gas age}(\rho_{\text{LID}}) = \frac{1}{1.367}\left(0.934 \times \frac{(\text{DCH})^2}{D^0_{CO_2}} + 4.05\right), \tag{3}$$

where DCH is the diffusive column height, defined as the lock-in depth minus a 3 m convective zone at the surface where firn air is well-mixed with the atmosphere. $D^0_{CO_2}$ is the free air diffusivity of CO_2 defined in Schwander et al. (1988) and Buizert et al. (2012). The lock-in depth is defined as the depth at which the effective molecular diffusivity of the gas is reduced to one thousandth of the free air diffusivity (Buizert et al., 2013).

3.3 Modeling Diffusion Length

The combined effects on the isotope profile due to diffusion and firn densification are given by:

$$\frac{\partial \delta}{\partial t} = D\frac{\partial^2 \delta}{\partial z^2} - \dot{\epsilon} z \frac{\partial \delta}{\partial z}, \tag{4}$$

where δ is the isotope ratio, D is the diffusivity coefficient, $\dot{\epsilon}$ is the vertical strain rate, and z is the vertical coordinate assuming an origin fixed on an arbitrary sinking layer of firn (Johnsen, 1977; Whillans and Grootes, 1985).

The diffusivity coefficient D_x of each isotope x depends on the temperature and density profile of the firn column Whillans and Grootes (1985); Johnsen et al. (2000):

$$D_x = \frac{m\, p\, D_x^{air}}{RT\, \alpha_x\, \tau}\left(\frac{1}{\rho} - \frac{1}{\rho_{ice}}\right), \tag{5}$$

where m is the molar weight of water, p is the saturation pressure over ice at temperature T and with gas constant R, D_x^{air} is the diffusivity of each isotopologue through air, α_x is the fractionation factor for each isotopic ratio in water vapor over ice, τ is the tortuosity of the firn, ρ is the firn density, and ρ_{ice} is the density of ice. Values for these parameters are given in the Supporting Information.

Using the output from the firn-densification model, we calculate water-isotope diffusion through the depth-density profile. First, the density profile is used to calculate the diffusivity of each isotope based on Equation 5. We then solve for the diffusion length σ_{firn} of a particular isotope ratio in terms of its effective diffusivity coefficient D and the firn density ρ (Gkinis et al., 2014):

$$\sigma_{firn}^2(\rho) = \frac{1}{\rho^2} \int_{\rho_0}^{\rho} 2\rho^2 \left(\frac{d\rho}{dt}\right)^{-1} D(\rho) d\rho, \tag{6}$$

where ρ_0 is the surface density and $\frac{d\rho}{dt}$ is the material derivative of the density. To calculate the diffusivity D, we use an atmospheric pressure of 0.7 atm (Severinghaus et al., 2001), which we assume to be constant through time.

Cumulative vertical strain significantly thins layers in the ice. The thinning function is defined as the fractional amount of thinning that has occurred at a given depth in the ice sheet. We account for the effects of vertical strain on our modeled firn diffusion length, σ_{firn}, using a thinning function Γ. We model the diffusion length measured in the ice core as $\sigma_{icecore}$:

$$\sigma_{icecore} = \sigma_{firn} \times \Gamma. \tag{7}$$

Recall that when we compare the modeled diffusion length with the observations, the observations have been corrected for diffusion in solid ice.

3.4 Modeling Annual-Layer Thickness

Annual-layer thickness λ is given by the accumulation rate A multiplied by the thinning function Γ:

$$\lambda = A \times \Gamma. \tag{8}$$

4 Statistical Inverse Approach

We use a Bayesian statistical approach to produce an ensemble of possible solutions to our inverse problem. Through many iterations, we use the forward model described above to solve our forward problem and determine the range of possible model inputs. This forward problem is described by the following equation, where the forward model, G, calculates the modeled observables, or data parameters, d as a function of unknown input variables, or model parameters, m:

$$G(m) = d. \tag{9}$$

Our forward model G is nonlinear and cannot be solved analytically. Instead, we use a Monte Carlo approach to solve the inverse problem by testing many instances of m through the forward model G to find the output d that best matches the observations d_{obs}. The theory and practical implementation of this approach are detailed in the Supporting Information (Metropolis et al., 1953; Tarantola, 1987; Mosegaard and Tarantola, 1995; Gelman et al., 1996; Mosegaard, 1998; Khan et al., 2000; Mosegaard and Sambridge, 2002; Mosegaard and Tarantola, 2002; Steen-Larsen et al., 2010).

We incorporate *a priori* information about model parameters based on their modern values and our best guess of how they have varied through time. We include this *a priori* information by creating bounds on the allowable model space to explore. If the algorithm proposes a solution m_x that falls outside of our bounded model space, m_x is disregarded and another solution is evaluated.

We also determine initial guesses m_1 for each parameter. Initializing the problem at what is judged to be a reasonable solution m_1 helps to avoid non-physical solutions (MacAyeal, 1993; Gudmundsson and Raymond, 2008). We design initial guesses for each parameter that are simplified versions of our best initial guess, allowing higher-frequency information to be inferred from the optimization. The initial guess of temperature is a step-function version of the water-isotope record. The initial guess for the thinning function is the output of a Dansgaard and Johnsen (1969) (DJ) ice-flow model. This simple model produces an approximation of the dynamics acceptable at many ice-core sites (Hammer et al., 1978). We use a kink height of $h_0 = 0.2$ to simulate the flank flow at the SPC14 site. To produce an initial guess for accumulation rate, we divide the layer-thickness data by this thinning function and approximate the result with a simplified step function.

Each parameter is bounded based on naïve expectations for its variability. For temperature, we bound the model space with an upper and lower scaling of the step-function initial guess version of the water-isotope record. We create an envelope based on previous estimates of glacial-interglacial temperature change in Antarctica, which allows for solutions with glacial-interglacial changes as small as 0.5°C and as large as 15°C. For accumulation rate, the bounded model-parameter range is an envelope about our initial guess defined as ± 0.02 m yr^{-1}. Given the surface and Holocene accumulation-rate fluctuations at South Pole described in Lilien et al. (2018), this range is a reasonable limit on accumulation rate, while still allowing variation in the values tested in each m. For the ice-equivalent thinning function, we enforce a value of one at the surface but do not provide further constraints on the model space because it is effectively constrained by the bounds on accumulation rate and layer thickness.

5 *A posteriori* Results

5.1 Probability Distributions

The resulting solutions m from our inverse approach are described by the *a posteriori* distribution. To visualize the high-dimensional *a posteriori* distribution, we plot probability distributions for each parameter. Rather than create separate probability distributions for each of the many parameters in our model space, we plot each probability distribution successively in a single figure to visualize the entire model space at once. Figure 4 shows our results, with the model inputs on the left and outputs on the right. The grey shading shows successive probability distributions. A vertical slice through the shading in each plot represents the probability distribution for a particular parameter (recall that a parameter represents the value of a variable at a specified model timestep, *i.e.* the value of temperature at the 4th timestep). How often a particular value is accepted for each parameter is represented by the shading, where darker shading denotes values that were accepted more often. The solid magenta curves describe the initial guess for each parameter, and the dashed magenta curves describe the bounded model space (for temperature and accumulation rate). The right three panels of Figure 4 illustrate how well the modeled observables $d(m)$ match with the observations d_{obs} throughout the collection of solutions.

5.2 Sensitivity of Results

We evaluate the sensitivity of our results to different choices made in the formulation of the forward and inverse problems. Since we opted to keep the surface density ρ_0 in the firn-densification model constant through time, we tested the sensitivity of a change. We tested two alternate values of surface density $\rho_{surface}$ (450 kg m^{-3} and 550 kg m^{-3}); we find no significant change in the results. We also evaluated the sensitivity to different initial guesses for each parameter. Altering the initial guesses within the model space

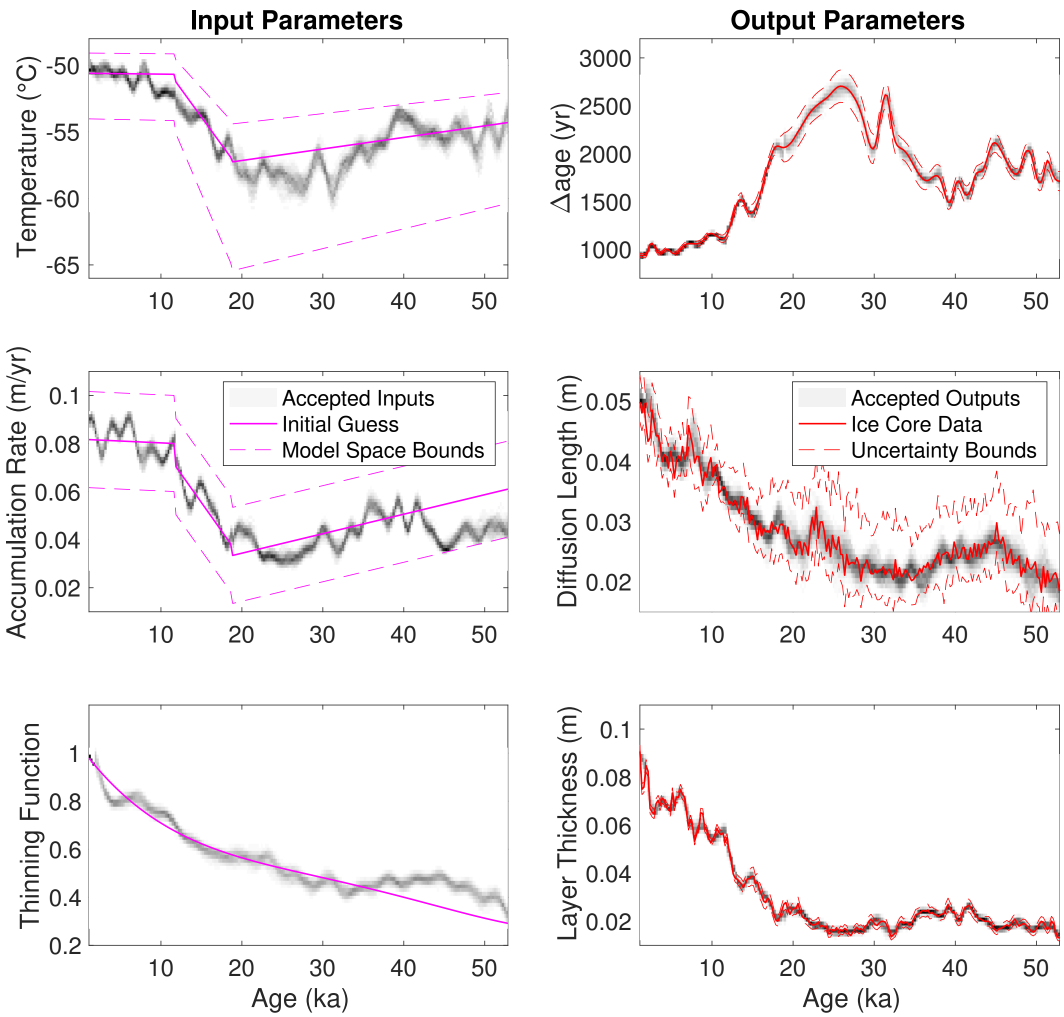

Figure 4: Results of the Monte Carlo inverse calculations, showing the *a posteriori* distribution result compared with *a priori* information. The grey shading in each panel represents probability distributions for each parameter from the *a posteriori* distribution, where darker shading signifies greater likelihood. Left panels show the initial guesses (solid magenta) and model bounds (dashed) for the input parameters: temperature, accumulation rate, and thinning. Right panels show the observational data (solid red) and prescribed uncertainties (dashed) for the output parameters: Δage, diffusion length, and layer thickness.

bounds do not affect the final results. Additionally, including higher-frequency *a priori* information in our initial guesses does not change the results. For example, we evaluated initial guesses of constant values for each of temperature, accumulation rate, and thinning function. These extremely simplified initial guesses produce results indistinguishable from those that include the high-frequency variability of each comparison data set, but require many more iterations to reach an equilibrium solution. As recommended in Gudmundsson and Raymond (2008), we opted for a middle-ground approach that saves time by setting the initial guess close to the expected answer but relies on the optimization to obtain high-frequency information. We also tested the sensitivity of the results to each data set individually, as detailed in the Supporting Information. One key conclusion from these tests is that all three data sets (Δage, layer thickness, and diffusion length) provide important information for producing a well-constrained result (Figure S3).

6 Discussion

Our reconstructions for accumulation rate, ice thinning, and temperature compare well with estimates from simpler calculations and independent data. In general, the results are in agreement with naïve expectations, but with some important differences. Because the accumulation-rate and thinning reconstructions are fundamentally linked through Equation 8, we discuss them together. We then compare our reconstruction for temperature with the traditional water-isotope paleothermometer, and discuss the broader implications of our results. The *a posteriori* distribution is near-Gaussian, and in this section we plot its mean and standard deviation rather than the full probability distributions. Recall that the *a posteriori* distribution comprises only accepted solutions, a subset of all iterations.

6.1 Accumulation Rate and Thinning Function

Figure 5 shows the results for the thinning function (panel (a)) and accumulation rate (panel (b)). The grey shading denotes a band of two s.d. of the *a posteriori* distribution. In general, thinning functions are expected to be smooth and to decrease monotonically because they integrate the total thinning experienced at a given depth, as illustrated by the results of a 1-D Dansgaard-Johnsen (DJ) model with $h_0 = 0.2$ (red curve, panel (a)). However, the SPC14 site is far from an ice divide such that variations in the bed topography upstream can create more complex thinning histories (e.g., Parrenin et al., 2004). Thus, the thinning function result is similar to the DJ-model output, but contains additional higher-frequency variations. To evaluate the plausibility of these variations in the primary reconstruction, we compare with two other independent estimates of the thinning function, an ice-flow-model thinning function and a δ^{15}N-based thinning function.

First, we compare the primary thinning function with one calculated from an ice-flow model. We use a 2.5-D flowband model (Koutnik et al., 2016) forced with observations of the bedrock topography and the accumulation-rate pattern. Details of the model setup are given in the Supporting Information (Nye, 1963; Looyenga, 1965; Gades et al., 2000; Neumann et al., 2008; Catania et al., 2010; Jordan et al., 2018). The resulting thinning function is best considered in two segments. The thinning function for the past 10 ka (solid black line in Figure 5) is well constrained because the flowline is known (Lilien et al., 2018) and the bed topography has been measured along the flowline (Figure S6). The key result is that the bed undulations along the flowline cause the same structure as is inferred in the primary thinning function. The "reversal" in the thinning function at 7 ka, where deeper layers have thinned less than shallower layers, matches well in both the primary and ice-flow-model thinning functions. This feature is caused by an overdeepening in the bed topography (Figure S10).

For ages older than 10 ka, we do not know where the ice originated and thus cannot use the ice-flow model to determine the thinning function with confidence. Instead, we aim to evaluate whether the primary thinning function is physically plausible, given what we know about the bed topography in the region. Using airborne radar measurements (Forsberg et al., 2017) to guide a simulated but realistic bed, we show that the ice-flow model (black dashed line) can approximately match the magnitude and structure of the primary thinning function. Therefore, the primary thinning function is consistent with expectations, given plausible variations in bedrock topography.

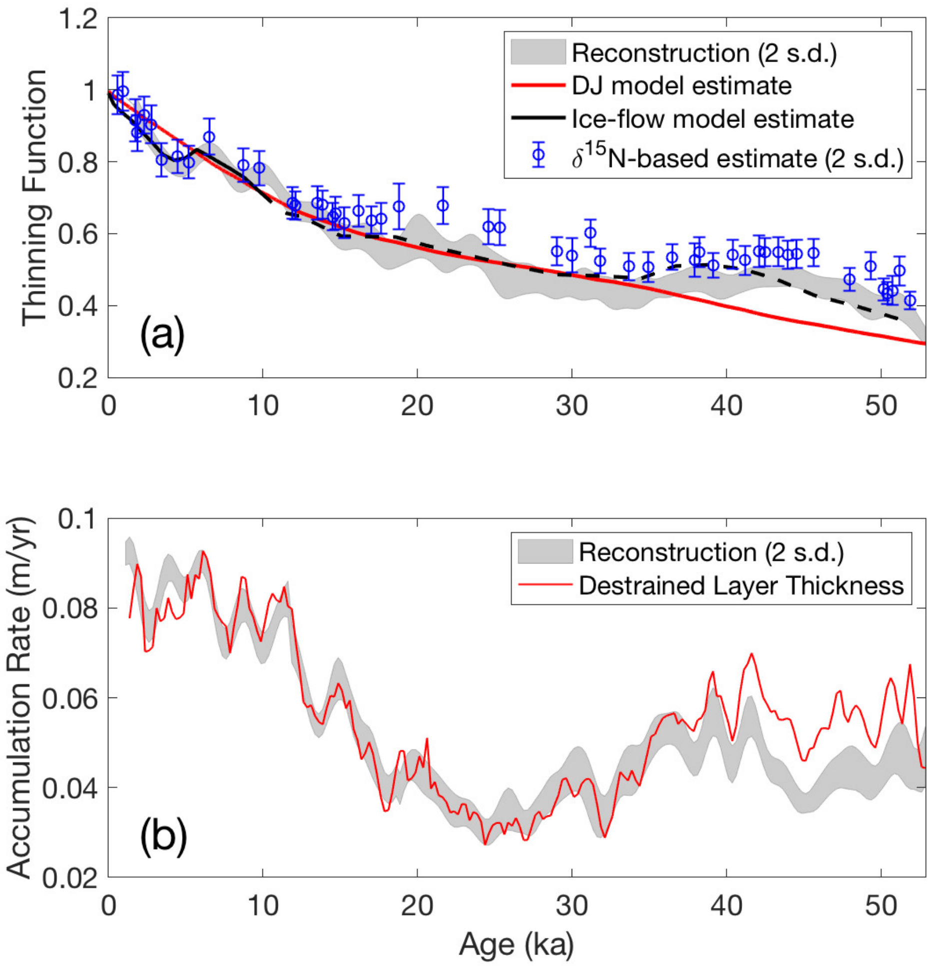

Figure 5: Reconstructions of accumulation rate and thinning function for SPC14. Two s.d. (grey shading) of the *a posteriori* distribution is plotted for each reconstruction alongside comparison estimates. Panel (a) shows the primary thinning function reconstruction (grey) compared to a DJ-model output with $h_0 = 0.2$ (red), an ice-flow-model thinning function from a 2.5-D flowband model (black), and a δ^{15}N-based thinning function with error bars showing two s.d. uncertainty (blue). The solid black curve shows where the ice-flow-model thinning function is well constrained by data, and the dashed black curve shows where the bed topography is simulated. Panel (b) shows the accumulation-rate reconstruction compared to the layer-thickness data destrained by the same DJ-model output (red).

Second, we compare the primary thinning function with a δ^{15}N-based thinning function (blue line; error bars show two s.d. uncertainty). We obtain this estimate using measurements of the δ^{15}N of N_2 gas, data reported in Winski et al. (2019), following the methods described in Parrenin et al. (2012). The enrichment of δ^{15}N in the ice core is a linear function of the original diffusive column height (DCH) of the firn due to the signal of gravitational fractionation recorded at the lock-in depth (LID) (Sowers et al., 1992; Buizert et al., 2013). To determine the thinning that has occurred in the ice sheet, the ice-equivalent LID is compared to the "Δdepth" of the ice core, which reflects the thickness of ice that originally comprised the firn column at the ice-sheet surface. The Δdepth is closely related to the Δage and is the difference in depth in the ice core of the same climate event. The thinning function Γ is then given by (Parrenin et al., 2012):

$$\Gamma = \frac{\Delta\text{depth}}{A \times \text{LID}}, \tag{10}$$

where A is a scaling factor that accounts for the ice-equivalent thickness of the original firn column (Winski et al., 2019). Full details on this approach and its uncertainties are given in the Supporting Information.

Figure 5 panel (a) shows that the structure of the δ^{15}N-based thinning function agrees well with the primary reconstruction, showing the same high-frequency variations and mean estimates whose error bars overlap. At ages greater than about 15 ka, the δ^{15}N-based thinning function appears shifted towards higher values (less thinning) on average. Differences between firn-model results and constraints from δ^{15}N have previously been note for sites at very cold temperatures (Freitag et al., 2013; Bréant et al., 2017); this has been referred to colloquially as the "δ^{15}N problem". The agreement between our primary reconstruction and the Δdepth calculation shows that at least at South Pole, this discrepancy is within the uncertainties on both. We emphasize that the uncertainties for the Δdepth calculation are not depth-independent; many known sources of error are expected to be systematic. For example, if the WAIS Divide Δage data set were systematically too large during the glacial period, correcting for this would result in smaller estimates for the SPC14 Δdepth, and therefore smaller values (more thinning) in the δ^{15}N-based thinning function. The same adjustment to Δage results in no significant change in the primary thinning function, thus improving the agreement between the means of the two independent estimates. Similarly, the scaling factor of A in Equation 10, whose mean value is taken from modern observations of the firn column, is unlikely to be constant in time; this would also systematically affect the δ^{15}N-based thinning function without changing the results of our primary reconstruction.

For comparison with the accumulation-rate reconstruction, Figure 5 panel (b) shows the raw annual-layer thickness data corrected for thinning from the 1-D DJ-model output (red curve). We note that high-frequency variability in the accumulation-rate reconstruction is limited by our enforcing smooth perturbations at each iteration (see Supporting Information). The low-frequency variability, on the other hand, reflects new information resulting from the optimization. In particular, the thinning function reversal between 40 and 50 ka is reflected by a significantly smaller accumulation rate than would be inferred using a DJ model.

To produce an estimate of the accumulation-rate history that incorporates the high-frequency information of the SPC14 timescale (Winski et al., 2019) and is also consistent with the thinning results discussed above, we combine information from all available measurements (Figure 6). We destrain the SP19 layer thicknesses using the mean of the primary thinning function and the δ^{15}N-based thinning function. We determine uncertainty for this estimate (two s.d.) by destraining the layer-thickness data with the uncertainty bounds of each thinning function (blue and red representing the primary and δ^{15}N-based thinning functions, respectively). This represents our best estimate for the accumulation-rate history in SPC14.

6.2 Temperature Reconstruction

The temperature reconstruction is shown in Figure 7. For comparison, we show two scaled versions of the measured δ^{18}O, corrected for secular variations in the δ^{18}O of sea-water, following Bintanja and van de Wal (2008). Recall that while we used diffusion length determined from the δ^{18}O power spectrum in our reconstruction, we do not use the δ^{18}O

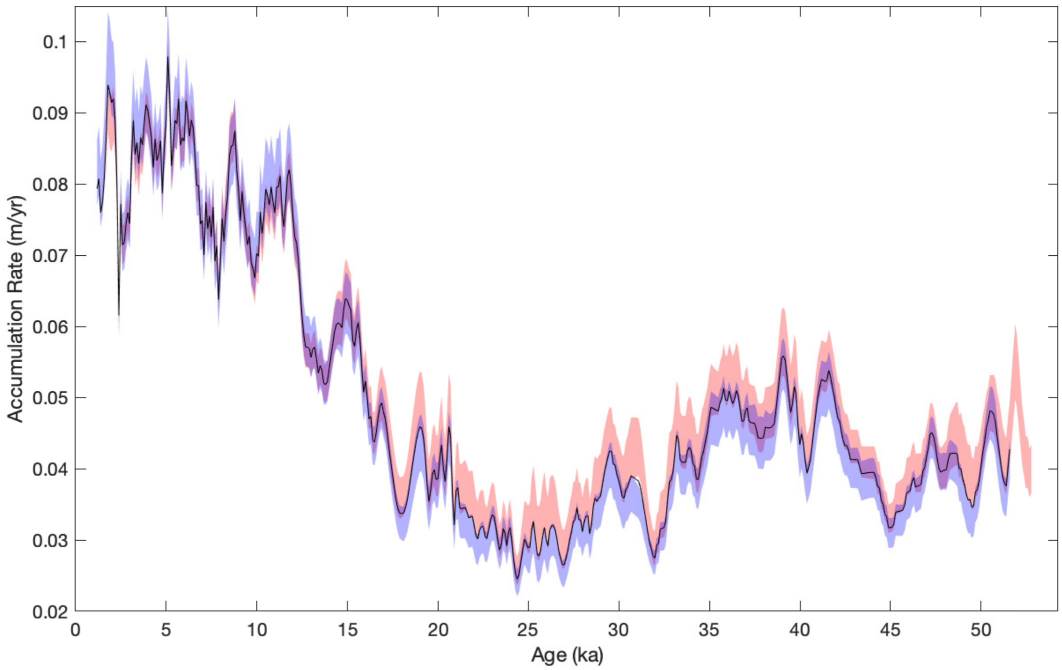

Figure 6: Accumulation rate in SPC14, averaged to 100-year resolution. The accumulation rate (black line) is calculated from the layer-thickness data divided by the mean of the primary and δ^{15}N-based thinning functions shown in Figure 5(a). Also shown is the uncertainty (2 s.d.) as calculated individually from the primary thinning function (red) and the δ^{15}N-based thinning function (blue).

values; hence, these comparisons serve as an independent calibration of the traditional water-isotope thermometer, similar to what has been done previously with borehole thermometry (Cuffey et al., 1995, 2016) but maintaining higher-frequency information. The red curve in Figure 7 uses a scaling of $\partial(\delta^{18}\text{O})/\partial T = 0.8‰{}^\circ\text{C}^{-1}$, which is both the observed modern surface isotope-temperature relationship at the site (Fudge et al., 2020) and the value commonly used in the literature for Antarctica (e.g. Jouzel et al., 2003; Masson-Delmotte et al., 2008). The black curve shows the best-fit linear relationship between δ^{18}O and the mean of our reconstruction; this has a significantly greater slope of $0.98‰{}^\circ\text{C}^{-1}$.

A single $\partial(\delta^{18}\text{O})/\partial T$ scaling does not capture all of the variability in our T reconstruction. Nevertheless, the overall agreement is excellent, and there is no evidence of the large change in scaling that has been observed in Greenland ice cores (Cuffey et al., 1995) and attributable primarily to changes in the seasonality of precipitation (Steig et al., 1994; Werner et al., 2000). The correlation coefficient between δ^{18}O and the mean of our ensemble is 0.93. As already noted and as is apparent in Figure 7, our calibration yields a significantly greater slope than has been generally used in previous work. This is consistent with isotope-modeling results that show that the sensitivity of δ^{18}O to temperature should increase at sites with colder mean-annual temperatures and higher elevations in Antarctica. For example, Markle (2017) obtains $\partial(\delta^{18}\text{O})/\partial\ \text{T} \sim 0.8‰{}^\circ\text{C}^{-1}$ for a location like WAIS Divide, in agreement with the borehole temperature calibration, and $\partial(\delta^{18}\text{O})/\partial\ \text{T} \sim\ 1‰{}^\circ\text{C}^{-1}$ for South Pole. This difference in sensitivity occurs because air masses traveling to higher elevations are on different moist isentropic surfaces, and experience greater rainout for a given change in temperature (Bailey et al., 2019).

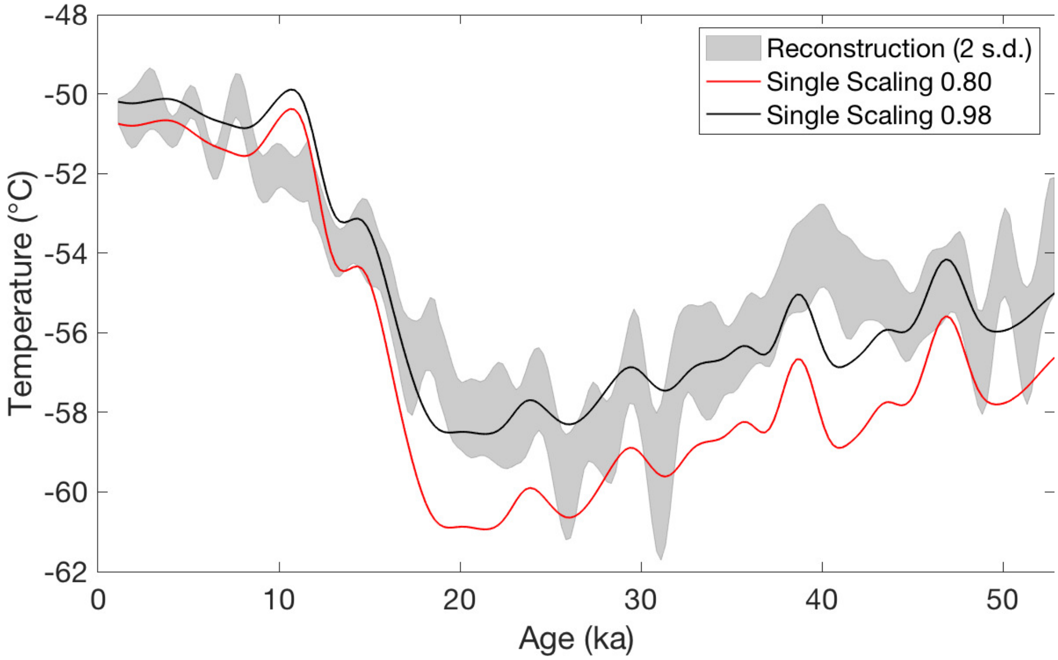

Figure 7: Reconstruction of temperature and relationship with δ^{18}O. Grey shading shows two s.d. of the *a posteriori* distribution. Solid lines show scaled versions of the δ^{18}O, discretely averaged to 250-year resolution and smoothed with a 3000-year lowpass filter. The water isotopes are scaled by 0.8‰°C^{-1}, the modern surface relationship (red), and by 0.98‰°C^{-1}, the calibrated linear relationship with the mean of the temperature reconstruction (black).

We use our temperature reconstruction to determine the magnitude of glacial-interglacial temperature change at South Pole. We define this change as the difference in the mean temperature within the intervals of 0.5 - 2.5 ka and 19.5 - 22.5 ka. Note that our reconstruction ends at 0.5 ka, not the present, because the upper ∼500 years of the record is in the firn; hence, Δage is undefined and diffusion of water isotopes is still in progress. The choice of the last glacial maximum (LGM) window avoids the prominent warming of the Antarctic Isotope Maximum (AIM2) event. Our mean reconstruction for SPC14 yields a change of 7.5±0.8°C (one s.d.). However, because SPC14 was drilled far from the divide, deeper ice in the core originated increasingly farther upstream. We can correct for this using modern ice-flow data and surface observations. Fudge et al. (2020) show that the magnitude of the adjustment, based on observations of the δ^{18}O surface gradient and surface-temperature lapse rate of 10°C km^{-1}, is roughly a 1°C warming correction in the glacial period. Thus, our best estimate for the glacial-interglacial temperature change at the South Pole site is 6.3±0.8°C (one s.d.). We show the ice-flow-corrected, calibrated δ^{18}O record in Figure 8; this should be considered the best current estimate of temperature-calibrated isotope variations at South Pole through the last 54,000 years. We calculate the uncertainty (two s.d.) by taking into account the correlation coefficient between the reconstruction and the scaled-isotope estimate.

Our results from SPC14 indicate a 2 to 3.5°C lower glacial-interglacial surface temperature change than reconstructed from other ice cores in east Antarctica, which is generally taken to be 9°C (Parrenin et al., 2013). This difference cannot readily be attributed to elevation change at South Pole, which is unlikely to have been more than 100 m thinner during the last glacial maximum (e.g., Pollard and DeConto, 2009), thus account-

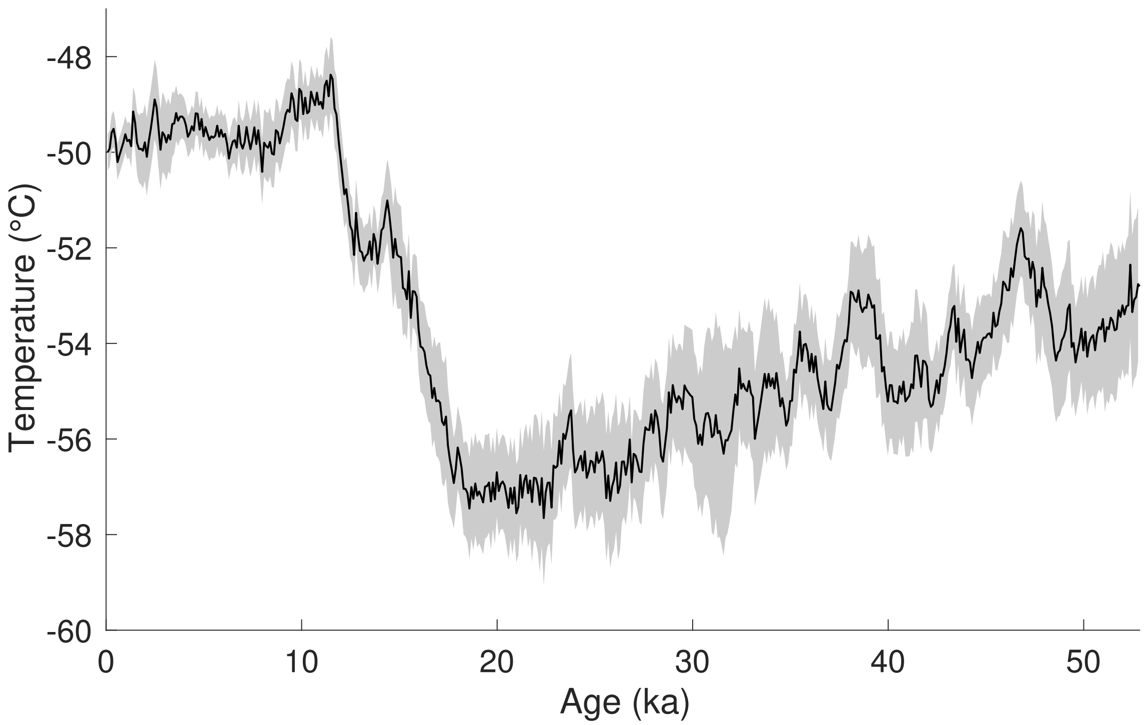

Figure 8: Advection-corrected temperature at South Pole, from scaled δ^{18}O, averaged to 100-year resolution. The δ^{18}O is scaled by 0.98‰°C^{-1}, the best-fit relationship with the independent temperature reconstruction from our inverse method, and corrected for ice flow following Fudge et al. (2020). Uncertainty (two s.d.) takes into account the correlation coefficient between the temperature reconstruction and the scaled-isotope estimate.

ing for at most about 1°C of the difference. Instead, we suggest that the commonly-used 9°C value, which is based on water isotopes unconstrained by the independent estimates we use here, is too large. Importantly, this may resolve an apparent disagreement, first recognized at least three decades ago (Crowley and North, 1991), between ice-core based temperature estimates and results from general circulation models (GCMs), which do not produce cold-enough LGM temperatures unless surface elevations significantly higher than present are assumed (e.g., Masson-Delmotte et al., 2006; Schoenemann et al., 2014; Masson-Delmotte et al., 2013). Such GCM estimates are in better agreement with our results if corrected for the prescribed elevation changes, consistent with the smaller changes in East Antarctic ice elevations during the LGM indicated by more recent results (Briggs et al., 2014; Argus et al., 2014; Roy and Peltier, 2015) than those suggested by earlier work (e.g., Peltier, 2004).

7 Conclusions

The South Pole ice core (SPC14) provides the opportunity to obtain reconstructions of important climate variables using multiple independent constraints. SPC14 has an empirical measure of the gas-age ice-age difference, Δage, obtained independent of firn densification modeling (Epifanio et al., 2020). We also present a new continuous record of water-isotope diffusion length. Both Δage and diffusion length depend on firn properties, which in turn depend on the snow-accumulation rate and firn temperature. The water-isotope diffusion length provides an important additional constraint on the ice-thinning function, which relates measured layer thickness with the original accumulation rate at the surface. Layer thickness variations in SPC14 are well-constrained by the ice timescale for the core, developed by annual-layer counting through the Holocene and by stratigraphic matches with the well-dated West Antarctic Ice Sheet Divide ice core (Winski et al., 2019). We have used a statistical inverse approach to combine information from all these data sets to obtain an ensemble of self-consistent temperature, accumulation-rate, and ice-thinning histories.

Our estimate of the thinning function for SPC14 indicates greater variations in thinning rate, and significantly less thinning at depth, than can be captured with a simple one-dimensional ice-flow parameterization such as the commonly-used Dansgaard-Johnsen model. Variations in thinning comparable in timing and magnitude to our results are supported by a 2.5-D flowband model that accounts for variations in bedrock topography upstream of the drill site. Our results are further supported by measurements of the δ^{15}N of N_2, which provide an additional independent estimate of thinning, based on the "Δdepth" calculation of firn-layer thickness following Parrenin et al. (2012). The thinning function reconstruction is particularly important because SPC14 was drilled more than 200 km away from the ice divide and the surface velocity is high (10 m yr^{-1}) (Casey et al., 2014).

Our temperature reconstruction serves two important purposes. First, it provides the first empirical, high-frequency estimate of temperature for an East Antarctic ice-core site that does not depend on the traditional water-isotope paleothermometer. It thus enables an independent calibration of the isotope-temperature sensitivity, $\partial(\delta^{18}\mathrm{O})/\partial T$, similar to what has been done in central Greenland and in West Antarctica using borehole thermometry (Cuffey et al., 1995, 2016). Moreover, our approach preserves additional high-frequency information that is not available from the highly diffused borehole-temperature measurements. Second, our result demonstrates a smaller glacial-interglacial temperature change than previously estimated elsewhere in East Antarctica. This smaller glacial-interglacial change may resolve the discrepancy between temperature estimates from climate models and ice-core data that has been noted in the literature for more than three decades (Crowley and North, 1991). Our results thus lend greater confidence to the fidelity of climate-model simulations of last glacial maximum climate.

Acknowledgments

This work was funded through grants from the US National Science Foundation (E.J.S. (1143105 and 1141839), C.B. (1643394 and 1443472), M.R.K. and others (1443471)). We thank J.P. Severinghaus for providing ^{15}N data collected under grant NSF1443710. The SPC14 high-resolution water stable isotope record published with this paper can be accessed through the USAP Data Center (DOI: 10.15784/601239). The radar data used in the ice-flow modeling can be accessed through the USAP Data Center at https://www.usap-dc.org/view/project/p0000200. We thank G.H. Roe, B.R. Markle, and D. Shapero for suggestions on this work, and M. Twickler and J. Souney for their work administering the SPICEcore project. We thank the SPICEcore field team, the 109th New York Air National Guard, and the National Science Foundation Ice Core Facility, for the collection, transport, processing, and storage of the core.

References

Argus, D.F., Peltier, W.R., Drummond, R. and Moore, A.W.(2014) The Antarctica component of postglacial rebound model ICE-6G C (VM5a) based upon GPS positioning, exposure age dating of ice thicknesses, and relative sea level histories. *Geophys. J. Int.*, 198(1), 537-563, doi:10.1093/gji/ggu140.

Bailey, A., Singh, H.K.A., and J. Nusbaumer. (2019). Evaluating a Moist Isentropic Framework for Poleward Moisture Transport: Implications for Water Isotopes Over Antarctica. *Geophysical Research Letters*, 46(13), 7819–7827.

Barkan, E and Luz, B. (2007). Diffusivity fractionations of $H_2^{16}O/H_2^{17}O$ and $H_2^{16}O/H_2^{18}O$ in air and their implications for isotope hydrology. *Rapid Communications in Mass Spectrometry*, 21(18), 2999-3005.

Bazin, L., Landais, A., Lemieux-Dudon, B., Toyé Mahamadou Kele, H., Veres, D., Parrenin, F., Martinerie, P., Ritz, C., Capron, E., Lipenkov, V., Loutre, M.-F., Raynaud, D., Vinther, B., Svensson, A., Rasmussen, S. O., Severi, M., Blunier, T., Leuenberger, M., Fischer, H., Masson-Delmotte, V., Chappellaz, J., and Wolff, E. (2013). An optimized multi-proxy, multi-site Antarctic ice and gas orbital chronology (AICC2012): 120800 ka. *Climate of the Past*, 9, 1715-1731.

Bintanja, R., and van de Wal, R. S. W. (2008). North American ice-sheet dynamics and the onset of 100,000-year glacial cycles. *Nature*, 454(7206), 869.

Blunier, T., and Schwander, J. (2000). Gas enclosure in ice: age difference and fractionation. *Physics of Ice Core Records* 307–326. Hokkaido University Press.

Bréant, C., Martinerie, P., Orsi, A., Arnaud, L., and Landais, A. (2017). Modelling firn thickness evolution during the last deglaciation: constraints on sensitivity to temperature and impurities. *Climate of the Past*, 13, 833-853.

Briggs, R.D. , Pollard, T., and Tarasov, L. (2014). A data-constrained large ensemble analysis of Antarctic evolution since the Eemian. *Quaternary Science Reviews*, Volume 103, 1 November 2014, 91–115, doi:10.1016/j.quascirev.2014.09.003

Buizert, C., Martinerie, P., Petrenko, V. V., Severinghaus, J. P., Trudinger, C. M., Witrant, E., Steele, L. P. et al. (2012). Gas transport in firn: multiple-tracer characterisation and model intercomparison for NEEM, Northern Greenland. *Atmospheric Chemistry and Physics*, 12(9), 4259–4277.

Buizert, C., Sowers, T., and Blunier, T. (2013). Assessment of diffusive isotopic fractionation in polar firn, and application to ice core trace gas records. *Earth and Planetary Science Letters*, 361, 110–119.

Buizert, C., Gkinis, V., Severinghaus, J. P., He, F., Lecavalier, B. S., Kindler, P., Brook, E. J., et al. (2014). Greenland temperature response to climate forcing during the last deglaciation. *Science*, 345(6201), 1177–1180.

Buizert, C., Cuffey, K. M., Severinghaus, J. P., Baggenstos, D., Fudge, T. J., Steig, E. J., Sowers, T. A. et al. (2015). The WAIS divide deep ice core WD2014 chronologyPart 1: methane synchronization (6831 kaBP) and the gas ageice age difference. *Climate of the Past*, 11(2).

Casey, K. A., Fudge, T. J., Neumann, T. A., Steig, E. J., Cavitte, M. G. P., and Blankenship, D. D. (2014). The 1500 m South Pole ice core: Recovering a 40 ka environmental record. *Annals of Glaciology*, 55(68), 137–146.

Catania, G, C. Hulbe, and H. Conway, 2010. Grounding-line basal melt rates determined using radar-derived internal stratigraphy, *J. Glaciol.* 56(197), 545-554.

Crowley, T. J., and G. R. North (1991). *Paleoclimatology.* New York, NY: Oxford University Press.

Cuffey, K. M., Clow, G. D., Alley, R. B., Stuiver, M., Waddington, E. D., and Saltus, R. W. (1995). Large arctic temperature change at the Wisconsin-Holocene glacial transition. *Science*, 270(5235), 455–458.

Cuffey, K. M. and Steig, E. J. (1998). Isotopic diffusion in polar firn: Implications for interpretation of seasonal climate parameters in ice-core records, with emphasis on central Greenland. *Journal of Glaciology*, 44(147), 273–284.

Cuffey, K. M., Clow, G. D., Steig, E. J., Buizert, C., Fudge, T. J., Koutnik, M., Severinghaus, J. P. et al. (2016). Deglacial temperature history of West Antarctica. *Proceedings of the National Academy of Sciences*, 113(50), 14249–14254.

Dahl-Jensen, D., Mosegaard, K., Gundestrup, N., Clow, G. D., Johnsen, S. J., Hansen, A. W., and Balling, N. (1998). Past temperatures directly from the

Greenland ice sheet. *Science*, 282(5387), 268–271.
Dansgaard, W. (1964). Stable isotopes in precipitation. *Tellus B*, 16(4), 436–468.
Dansgaard, W., and Johnsen, S. J. (1969). A flow model and a time scale for the ice core from Camp Century, Greenland. *Journal of Glaciology*, 8(53), 215–223.
Epifanio, J. A., Brook, E. J., Buizert, C., Edwards, J. S., Sowers, T. A., Kahle, E. C., Severinghaus, J. P., Steig, E. J., Winski, D. A., Osterberg, E. C., Fudge, T. J., Aydin, M., Hood, E., Kalk, M., Kreutz, K. J., Ferris, D. G., and Kennedy, J. A.: The SP19 chronology for the South Pole Ice Core - Part 2: gas chronology, Δage, and smoothing of atmospheric records, Clim. Past Discuss., https://doi.org/10.5194/cp-2020-71, 2020.
EPICA Community Members. 2004. Eight glacial cycles from an Antarctic ice core. *Nature* 429, 623–628.
Fausto, R. S., Box, J. E., Vandecrux, B. R. M., van As, D., Steffen, K., MacFerrin, M. J., Charalampidis, C. et al. (2018). A snow density dataset for improving surface boundary conditions in Greenland ice sheet firn modeling. *Frontiers in Earth Science*, 6(51).
Forsberg, R., A.V. Olesen, F. Ferraccioli, T. Jordan, H, Corr and K. Matsuoka (2017). PolarGap 2015/16: Filling the GOCE polar gap in Antarctica and ASIRAS flight around South Pole. Radar grids available at: $ftp : //ftp.bas.ac.uk/tomj/PolarGAP/PolarGAP\_radar\_grids.zip$
Freitag, J., Kipfstuhl, S., Laepple, T., and Wilhelms, F. (2013). Impurity-controlled densification: a new model for stratified polar firn. *Journal of Glaciology*, 59(218), 1163–1169.
Fudge, T. J., Waddington, E. D., Conway, H., Lundin, J. M. D., and Taylor, K. (2014). Interpolation methods for Antarctic ice-core timescales: application to Byrd, Siple Dome and Law Dome ice cores. *Climate of the Past*, 10(3), 1195–1209.
Fudge, T. J., Markle, B. R., Cuffey, K. M., Buizert, C., Taylor, K. C., Steig, E. J., Koutnik, M. et al. (2016). Variable relationship between accumulation and temperature in West Antarctica for the past 31,000 years. *Geophysical Research Letters*, 43(8), 3795–3803.
Fudge, T. J., Lilien, D. A., Koutnik, M., Conway, H., Stevens, C. M., Waddington, E. D., Steig, E. J., Schauer, A. J., and Holschuh, N. (2020). Advection and non-climate impacts on the South Pole Ice Core. *Clim. Past*, 16, 819832.
Gades, A.M., C.F. Raymond, H. Conway and R.W. Jacobel, 2000. Bed properties of Siple Dome and adjacent ice streams West Antarctica, inferred from radio-echo sounding measurements. *Journal of Glaciology*, 46(152), 88-94.
Gelman, A., Roberts, G. O., and Gilks, W. R. (1996). Efficient Metropolis jumping rules. *Bayesian Statistics*, 5(599-608), 42.
Gkinis, V., Simonsen, S. B., Buchardt, S. L., White, J. W. C. and Vinther, B. M. (2014). Water isotope diffusion rates from the NorthGRIP ice core for the last 16,000 years - glaciological and paleoclimatic implications. *Earth and Planetary Science Letters*, 405, 132–141.
Gudmundsson, G. H., and Raymond, M. (2008). On the limit to resolution and information on basal properties obtainable from surface data on ice streams. *The Cryosphere*, 2(3), 413–445.
Guillevic, M., Bazin, L., Landais, A., Kindler, P., Orsi, A., Masson-Delmotte, V., Martinerie, P. et al. (2013). Spatial gradients of temperature, accumulation and delta18O-ice in Greenland over a series of Dansgaard-Oeschger events. *Climate of the Past*, 9(3), 1029–1051.
Hammer, C. U., Clausen, H. B., Dansgaard, W., Gundestrup, N., Johnsen, S. J., and Reeh, N. (1978). Dating of Greenland ice cores by flow models, isotopes, volcanic debris, and continental dust. *Journal of Glaciology*, 20(82), 3–26.
Herron, M. M., and Langway, C. C. (1980). Firn densification: an empirical model. *Journal of Glaciology*, 25(93), 373–385.

Holme, C., Gkinis, V., and Vinther, B. M. (2018). Molecular diffusion of stable water isotopes in polar firn as a proxy for past temperatures. Geochimica et Cosmochimica Acta, 225, 128-145.

Huber, C., Leuenberger, M., Spahni, R., Flückiger, J., Schwander, J., Stocker, T. F., Jouzel, J. et al. (2006). Isotope calibrated Greenland temperature record over Marine Isotope Stage 3 and its relation to CH4. *Earth and Planetary Science Letters*, 243(3-4), 504–519.

Johnsen, S. J. (1977). Stable isotope homogenization of polar firn and ice. *Isotopes and Impurities in Snow and Ice*, 201–219.

Johnsen, S. J., Clausen, H. B., Cuffey, K. M., Hoffmann, G., Schwander, J. and Creyts, T. (2000). Diffusion of stable isotopes in polar firn and ice: The isotope effect in firn diffusion. *Physics of Ice Core Records*, 121–140.

Jones, T. R., Cuffey, K. M., White, J. W. C., Steig, E. J., Buizert, C., Markle, B. R., McConnell, J. R. and Sigl, M. (2017a). Water isotope diffusion in the WAIS Divide ice core during the Holocene and last glacial. *Journal of Geophysical Research: Earth Surface*, 122, 290-309.

Jones, T. R., White, J. W. C., Steig, E. J., Vaughn, B. H., Morris, V., Gkinis, V., Markle, B. R. and Schoenemann, S. W. (2017b). Improved methodologies for continuous flow analysis of stable water isotopes in ice cores. *Atmospheric Measurement Techniques*, 10, 617-632.

Jordan, T. A., Martin, C., Ferraccioli, F., Matsuoka, K., Corr, H., Forsberg, R., Olesen, A., and Siegert, M. (2018). Anomalously high geothermal flux near the South Pole. *Scientific reports*, 8(1), 1-8.

Jouzel, J., Barkov, N. I., Barnola, J. M., Bender, M., Chappellaz, J., Genthon, C., Raynaud, D. et al. (1993). Extending the Vostok ice-core record of palaeoclimate to the penultimate glacial period. *Nature*, 364(6436), 407.

Jouzel, J., Vimeux, F., Caillon, N., Delaygue, G., Hoffmann, G., MassonDelmotte, V., and Parrenin, F. (2003). Magnitude of isotope/temperature scaling for interpretation of central Antarctic ice cores. *Journal of Geophysical Research: Atmospheres*, 108(D12).

Jouzel, J., Masson-Delmotte, V., Cattani, O., Dreyfus, G., Falourd, S., Hoffmann, G., Fischer, H. et al. (2007). Orbital and millennial Antarctic climate variability over the past 800,000 years. *Science*, 317(5839), 793–796.

Kahle, E. C., Holme, C., Jones, T. R., Gkinis, V., and Steig, E. J. (2018). A Generalized Approach to Estimating Diffusion Length of Stable Water Isotopes From IceCore Data. *Journal of Geophysical Research: Earth Surface*, 123(10), 2377–2391.

Kahle, E. C. (2020). Climate reconstructions from ice cores: New techniques to understand the information preserved in the South Pole ice core (Doctoral dissertation, University of Washington, Seattle, USA).

Khan, A., Mosegaard, K., and Rasmussen, K. L. (2000). A new seismic velocity model for the Moon from a Monte Carlo inversion of the Apollo lunar seismic data. *Geophysical Research Letters*, 27(11), 1591–1594.

Kindler, P., Guillevic, M., Baumgartner, M. F., Schwander, J., Landais, A., and Leuenberger, M. (2014). Temperature reconstruction from 10 to 120 kyr b2k from the NGRIP ice core. *Climate of the Past*, 10(2), 887–902.

Koutnik, M. R., Fudge, T. J., Conway, H., Waddington, E. D., Neumann, T. A., Cuffey, K. M., Taylor, K. C., et al. (2016). Holocene accumulation and ice flow near the West Antarctic Ice Sheet Divide ice core site. *Journal of Geophysical Research: Earth Surface*, 121(5), 907–924.

Lamb, K. D., Clouser, B. W., Bolot, M., Sarkozy, L., Ebert, V., Saathoff, H., Mohler, O., and Moyer, E. J. (2017). Laboratory measurements of HDO/H2O isotopic fractionation during ice deposition in simulated cirrus clouds. *Proceedings of the National Academy of Sciences*, 114(22), 5612-5617.

Lazzara, M. A., Keller, L. M., Markle, T., and Gallagher, J. (2012). Fifty-year AmundsenScott South Pole station surface climatology. *Atmospheric Research*, 118, 240–259.

Lilien, D. A., Fudge, T. J., Koutnik, M. R., Conway, H., Osterberg, E. C., Ferris, D. G., and Stevens, C. M. et al. (2018). Holocene IceFlow Speedup in the Vicinity of the South Pole. *Geophysical Research Letters*, 45(13), 6557–6565.

Looyenga, H. (1965). Dielectric constants of heterogeneous mixtures. *Physica*, 31(3), 401–406.

Lorius, C., Jouzel, J., Raynaud, D., Hansen, J., and Le Treut, H. (1990). The ice-core record: climate sensitivity and future greenhouse warming. *Nature*, 347(6289), 139.

Luz, B., and Barkan, E. (2010). Variations of 17O/16O and 18O/16O in meteoric waters. *Geochimica et Cosmochimica Acta*, 74(22), 6276–6286.

MacAyeal, D. R. (1993). Binge/purge oscillations of the Laurentide ice sheet as a cause of the North Atlantic's Heinrich events. *Paleoceanography*, 8(6), 775–784.

Majoube, B. (1970). Fractionation factor of ^{18}O between water vapour and ice. *Nature* 226, 1242.

Markle, B. R. (2017). *Climate dynamics revealed in ice cores: advances in techniques, theory, and interpretation* (Thesis (PH. D.) – University of Washington, 208 pp.).

Martinerie, P., Lipenkov, V. Y., Raynaud, D., Chappellaz, J., Barkov, N. I., and Lorius, C. (1994). Air content paleo record in the Vostok ice core (Antarctica): A mixed record of climatic and glaciological parameters. *Journal of Geophysical Research*, 99(D5), 10565.

Masson-Delmotte, V., Kageyama, M., Braconnot, P., Charbit, S., Krinner, G., Ritz, C., and Gladstone, R. M. et al. (2006). Past and future polar amplification of climate change: climate model intercomparisons and ice-core constraints. *Climate Dynamics*, 26(5), 513–529.

Masson-Delmotte, V., Hou, S., Ekaykin, A., Jouzel, J., Aristarain, A., Bernardo, R. T., Frezzotti, M., et al. (2008). A review of Antarctic surface snow isotopic composition: Observations, atmospheric circulation, and isotopic modeling. *Journal of Climate*, 21(13), 3359–3387.

Masson-Delmotte, V., M. Schulz, A. Abe-Ouchi, J. Beer, A. Ganopolski, J.F. Gonzalez Rouco, E. Jansen, K. Lambeck, J. Luterbacher, T. Naish, T. Osborn, B. Otto-Bliesner, T. Quinn, R. Ramesh, M. Rojas, X. Shao and A. Timmermann (2013). Information from Paleoclimate Archives. In: Climate Change 2013: The Physical Science Basis. Contribution of Working Group I to the Fifth Assessment Report of the Intergovernmental Panel on Climate Change [Stocker, T.F., D. Qin, G.-K. Plattner, M. Tignor, S.K. Allen, J. Boschung, A. Nauels, Y. Xia, V. Bex and P.M. Midgley (eds.)]. *Cambridge University Press*, Cambridge, United Kingdom and New York, NY, USA.

Metropolis, N., Rosenbluth, A. W., Rosenbluth, M. N., Teller, A. H., and Teller, E. (1953). Equation of state calculations by fast computing machines. *The Journal of Chemical Physics*, 21(6), 1087–1092.

Monnin, E., Steig, E.J., Siegenthaler. U., Kawamura, K., Schwander, J., Stauffer, B., Morse, D.L., Stocker, T.F., Barnola, J.M., Bellier, B., Raynaud, D. and Fischer, H. (2004). Evidence for substantial accumulation rate variability in Antarctica during the Holocene through synchronization of CO_2 in the Taylor Dome, Dome C and DML ice cores. *Earth and Planetary Science Letters* 224, 45–54.

Mosegaard, K., and Tarantola, A. (1995). Monte Carlo sampling of solutions to inverse problems. *Journal of Geophysical Research: Solid Earth*, 100(B7), 12431–12447.

Mosegaard, K. (1998). Resolution analysis of general inverse problems through inverse Monte Carlo sampling. *Inverse Problems*, 14(3), 405.

Mosegaard, K., and Tarantola, A. (2002). Probabilistic approach to inverse problems. *International Geophysics Series*, 81(A), 237–268.

Mosegaard, K., and Sambridge, M. (2002). Monte Carlo analysis of inverse problems. *Inverse problems*, 18(3), R29.

Neumann, T.A., H. Conway, S. Price, E.D. Waddington and D.L. Morse, 2008. Holocene accumulation and ice-sheet dynamics in central West Antarctica. *J. Geophys. Res.*, 113, (F2).

Nye, J. (1963). Correction factor for accumulation measured by the thickness of the annual layers in an ice sheet. *Journal of Glaciology*, 4(36), 785788.

Parrenin, F., F. Remy, C., Ritz, M.J. Siegert, and J. Jouzel. (2004). New modeling of the Vostok ice flow line and implication of the glaciological chronology of the Vostok ice core. *Journal of Geophysical Research*, 109, (D20).

Parrenin, F., Barker, S., Blunier, T., Chappellaz, J., Jouzel, J., Landais, A., Veres, D. et al. (2012). On the gas-ice depth difference (Δdepth) along the EPICA Dome C ice core. *Climate of the Past*, 8(2), 1089–1131.

Parrenin, F., Masson-Delmotte, V., Kohler, P., Raynaud, D., Paillard, D., Schwander, J., Jouzel, J., et al. (2013). Synchronous change of atmospheric CO2 and Antarctic temperature during the last deglacial warming. *Science*, 339(6123), 1060–1063.

Peltier, W.R. (2004). Global Glacial Isostasy and the Surface of the Ice-Age Earth: The ICE-5G (VM2) Model and GRACE. *Ann. Rev. Earth and Planet. Sci.*, 32, 111–149.

Pollard, D., and DeConto, R. M. (2009). Modelling West Antarctic ice sheet growth and collapse through the past five million years. *Nature*, 458(7236), 329–332.

Price, P.B., O.V. Nagornov, R. Bay, D. Chirkin, Y. He,P. Miocinovic, A. Richards, K. Woschnagg, B. Koci and Victor Zagorodnov, 2002. Temperature Profile for Glacial Ice at the South Pole: Implications for Life in a Nearby Subglacial Lake. *Proceedings of the National Academy of Sciences*, 99(12), 7844-7847.

Raymond, C. (1983). Deformation in the vicinity of ice divides. *Journal of Glaciology*, 29(103), 357373.

Roy, K., and Peltier, W. R. (2015). Glacial isostatic adjustment, relative sea level history and mantle viscosity: reconciling relative sea level model predictions for the US East coast with geological constraints. *Geophysical Journal International*, 201(2), 1156–1181, doi:10.1093/gji/ggv066.

Severinghaus, J. P., Sowers, T., Brook, E. J., Alley, R. B., and Bender, M. L. (1998). Timing of abrupt climate change at the end of the Younger Dryas interval from thermally fractionated gases in polar ice. *Nature*, 391(6663), 141.

Severinghaus, J. P., Grachev, A., and Battle, M. (2001). Thermal fractionation of air in polar firn by seasonal temperature gradients. *Geochemistry, Geophysics, Geosystems*, 2(7).

Schoenemann, S. W., Steig, E. J., Ding, Q., Markle, B. R., and Schauer, A. J. (2014). Triple waterisotopologue record from WAIS Divide, Antarctica: Controls on glacialinterglacial changes in 17Oexcess of precipitation. *Journal of Geophysical Research: Atmospheres*, 119(14), 8741–8763.

Schwander, J., and Stauffer, B. (1984). Age difference between polar ice and the air trapped in its bubbles. *Nature*, 311(5981), 45–47.

Schwander, J., Stauffer, B., and Sigg, A. (1988). Air mixing in firn and the age of the air at pore close-off. *Annals of Glaciology*, 10, 141–145.

Schwander, J. The transformation of snow to ice and the occlusion of gases, in: H. Oeschger, C.C. Langway Jr. (Eds.), The Environmental Record in Glaciers and Ice Sheets, John Wiley, New York, 1989, pp. 53-67.

Sigl, M., Fudge, T. J., Winstrup, M., Cole-Dai, J., Ferris, D., McConnell, J. R., Bisiaux, M. et al. (2016). The WAIS Divide deep ice core WD2014 chronologyPart 2: Annual-layer counting (031 ka BP). *Climate of the Past*, 12(3), 769–786.

Simonsen, S. B., Johnsen, S. J., Popp, T. J., Vinther, B. M., Gkinis, V., and Steen-Larsen, H. C. (2011). Past surface temperatures at the NorthGRIP drill site from the difference in firn diffusion of water isotopes. *Climate of the Past*, 7(4), 1327.

Sowers, T., Bender, M., Raynaud, D., and Korotkevich, Y. S. (1992). δ15N of N2 in air trapped in polar ice: A tracer of gas transport in the firn and a possible constraint on ice agegas age differences. *Journal of Geophysical Research: Atmospheres*, 97(D14), 15683–15697.

Steen-Larsen, H. C., Waddington, E. D., and Koutnik, M. R. (2010). Formulating an inverse problem to infer the accumulation-rate pattern from deep internal layering in an ice sheet using a Monte Carlo approach. *Journal of Glaciology*, 56(196), 318–332.

Steig, E.J., Grootes, P.M., Stuiver, M. (1994). Seasonal precipitation timing and ice core records. *Science*, 266, 1885–1886.

Steig, E. J., Ding, Q., White, J. W. C., Küttel, M., Rupper, S. B., Neumann, T. A., Neff, P. D., Gallant, A. J. E., Mayewski, P. A., Taylor, K. C., Hoffmann, G., Dixon, D. A., Schoenemann, S., Markle B. M., Schneider, D. P., Fudge, T. J., Schauer, A. J., Teel, R. P., Vaughn, B., Burgener, L., Williams, J. and Korotkikh, E. (2013). Recent climate and ice-sheet change in West Antarctica compared to the past 2000 years. *Nature Geoscience*, *6*(5), 372.

Steig, E. J., Gkinis, V., Schauer, A. J., Schoenemann, S. W., Samek, K., Hoffnagle, J., Tan, S. M. et al. (2014). Calibrated high-precision 17O-excess measurements using cavity ring-down spectroscopy with laser-current-tuned cavity resonance. *Atmos. Meas. Tech.*, 7, 2421–2435.

Stevens, C. M., Verjans, V., Lundin, J. M. D., Kahle, E. C., Horlings, A. N., Horlings, B. I., and Waddington, E. D.: The Community Firn Model (CFM) v1.0, Geosci. Model Dev. Discuss., https://doi.org/10.5194/gmd-2019-361, in review, 2020.

Tarantola, A. (1987). Inverse problem theory: Methods for data fitting and model parameter estimation. *Elsevier*, Amsterdam.

van der Wel, G., Fischer, H., Oerter, H., Meyer, H., and Meijer, H. A. J. (2015). Estimation and calibration of the water isotope differential diffusion length in ice core records. The Cryosphere, 9(4), 1601-1616.

Veres, D., Bazin, L., Landais, A., Toyé Mahamadou Kele, H., Lemieux-Dudon, B., Parrenin, F., Chappellaz, J. et al. (2013). The Antarctic ice core chronology (AICC2012): an optimized multi-parameter and multi-site dating approach for the last 120 thousand years. *Climate of the Past*, 9(4), 1733–1748.

Werner, M., Mikolajewicz, U., Heimann, M., Hoffmann, G. (2000). Borehole versus isotope temperatures on Greenland: Seasonality does matter. *Geophysical Research Letters*, 27(5), 723–726.

Whillans, I. M., and Grootes P. M. (1985). Isotopic diffusion in cold snow and firn. *Journal of Geophysical Research*, 90(D2), 3910–3918.

Winski, D. A., Fudge, T. J., Ferris, D. G., Osterberg, E. C., Fegyveresi, J. M., Cole-Dai, J., Buizert, C., Epifanio, J., Brook. E.J., Beaudette. R., Severinghaus. J., Sowers. T., Steig, E.J., Kahle, E.C., Jones, T.R., Morris, V., Aydin, M., Nicewonger, M.R., Casey, K.A., Alley, R.B., Waddington, E.D., Iverson, N.A. (2019). The SP19 chronology for the South Pole Ice CorePart 1: volcanic matching and annual layer counting. *Climate of the Past*, 15(5), 1793–1808.